



**AIAA 94-1936  
COMPUTATIONAL  
AERODYNAMICS ANALYSIS OF  
FUTURE LAUNCH VEHICLE  
CONFIGURATIONS**

**B. VU**

**P. McCONNAUGHEY**

**NASA/Marshall Space Flight Center, AL**

**D. HUDDLESTON**

**Engineering Research Center**

**MSU, Starkville, MS**

**12th AIAA Applied Aerodynamics Conference**  
**June 20-22, 1994 / Colorado Springs, CO**



# COMPUTATIONAL AERODYNAMICS ANALYSIS OF FUTURE LAUNCH VEHICLE CONFIGURATIONS

B. Vu\*

P. McConnaughey\*\*  
NASA/MSFC, Huntsville, AL

D. Huddleston†  
Engineering Research Center  
MSU, Starkville, MS

## Abstract

An implicit finite volume high resolution scheme is applied for predicting three-dimensional, inviscid flow field over several launch vehicles including the National Launch System (NLS), the Single-Stage-To-Orbit (SSTO) lifting bodies, and wing-body vehicles. Simulations about NLS configurations were used to help benchmark Computational Fluid Dynamics (CFD) capabilities at NASA/MSFC. Likewise, simulations about SSTO were used to provide aerodynamic data to structure group to calculate structural wing loading for preliminary conceptual designs.

## Introduction

External flow computations have been conducted on several launch vehicle configurations. Among those selected for the study, the early heavy lift launch vehicle (EHLLV) is of primary interest. The second phase of the study is to support the advanced transportation technology program which takes place at Marshall Space Flight Center (MSFC) during the access-to-space study. The subsonic lift coefficients are calculated to determine at what speed and angle-of-attack a proposed lifting body will be able to land at, having structural and mission profile implications.

The grids are generated using a general purpose interactive grid generation system<sup>(1)</sup>. In most cases the computational mesh is formed using an appropriate algebraic method. The idea of using algebraic grid system is to preserve the grid clustering near the surface. Elliptic grid generation is only used to smooth out certain regions where the grids are skewed. A full three-dimensional (3-D) body with attached components, such as boosters,

wings, or winglets is also considered. In most cases the grids are generated in a single block and subsequently decomposed into several domains. In some cases the domain decomposition procedure helps ease the grid generation steps and keep the grid quality at an acceptable level.

The flow solver is based on an implicit finite volume implementation of Roe's approximate Riemann solver with higher order corrections as put forth by Osher and Chakravarthy<sup>(2)</sup> and implemented by Whitfield, for solving the unsteady, 3-D Euler and Navier-Stokes equations. The code has been applied to numerous practical problems including airfoil, wing and full aircraft simulations<sup>(3,4)</sup>. The numerical solutions obtained in the current study will be compared against those of Ames Research Center and test data from MSFC wind tunnel.

## Numerical Method

Arabshahi's<sup>(5)</sup> multi-block implementation of Roe upwind Euler/Reynolds-averaged Navier-Stokes solver developed by Whitfield<sup>(4)</sup>, and others at the Mississippi State University was applied to perform the simulations presented herein. This code, and other variants of the basic algorithm, has been used to successfully simulate numerous complex aerodynamic configurations. A brief description of the applied algorithm follows. A complete description of the theory, development and solver implementation is available in the cited references. Since all of the simulations presented herein are inviscid, viscous terms will be omitted in the following algorithm description.

For inviscid simulations, the code is used to solve the unsteady Euler equations in strong conservation form as

---

\* Aerospace Engineer, Member AIAA

\*\* Chief, CFD Branch, Member AIAA

† Research Engineer, Member AIAA

Copyright © 1994 by the American Institute of Aeronautics and Astronautics, Inc. No copyright is asserted in the United States under Title 17, U.S. Code. The U.S. Government has a royalty-free license to exercise all rights under the copyright claimed herein for the Governmental purposes. All other rights reserved by the copyright owner.

$$\frac{\partial \mathbf{q}}{\partial \tau} + \frac{\partial \mathbf{F}(\mathbf{q})}{\partial \xi} + \frac{\partial \mathbf{G}(\mathbf{q})}{\partial \eta} + \frac{\partial \mathbf{H}(\mathbf{q})}{\partial \zeta} = 0 \quad (1)$$

where the dependent variable vector,  $\mathbf{q}$ , and the inviscid flux vectors,  $\mathbf{F}$ ,  $\mathbf{G}$  and  $\mathbf{H}$ , are as presented in numerous references<sup>(e.g. 4,5,6)</sup>. Cell-centered finite-volume discretization is applied to (1) yielding the semi-discrete form

$$\frac{\partial \mathbf{q}}{\partial \tau} = - (\delta_i \mathbf{F} + \delta_j \mathbf{G} + \delta_k \mathbf{H}) \quad (2)$$

where the curvilinear grid spacing is taken as unity and the difference operator,  $\delta$ , is defined as, for example

$$\delta_i(\mathbf{F}) = \mathbf{F}_{i+\frac{1}{2}} - \mathbf{F}_{i-\frac{1}{2}} \quad (3)$$

Roe's approximate Riemann solver<sup>(9)</sup> is used to calculate the cell interface fluxes in (2). Following Whitfield<sup>(4)</sup> the Roe flux calculation across a cell face is expressed as a function of the left interface flux and the eigensystem of the so-called "Roe" matrix. For example, considering the flux across a  $\xi$  constant face, the first-order flux is given by

$$\bar{\mathbf{F}}_{i+\frac{1}{2}} = \mathbf{F}_i + \bar{\mathbf{A}}^- \left( \mathbf{q}_{i+\frac{1}{2}} - \mathbf{q}_{i-\frac{1}{2}} \right) \quad (4)$$

where

$$\bar{\mathbf{A}}^- = \mathbf{T} \mathbf{\Lambda}^- \mathbf{T}^{-1} \quad (5)$$

$\mathbf{T}$  and  $\mathbf{T}^{-1}$  denote the matrices formed from the right and left eigenvectors, respectively, and  $\mathbf{\Lambda}$  denotes the non-positive eigenvalues of the local "Roe" matrix. Higher order spatial accuracy is obtained by adding a corrective flux as proposed by Osher and Chakravarthy<sup>(7)</sup>.

Although the right-and-side is formed using flux-difference splitting, the applied implicit operator is developed based upon Steger-Warming<sup>(8)</sup> flux vector splitting theory. This does not provide a consistent linearization of the residual; however, it has been demonstrated that it does produce a more easily implemented algorithm while maintaining robustness and computational

efficiency<sup>(4)</sup>. To develop the implicit algorithm, the residual vector  $\mathbf{R}$  is split according to

$$\mathbf{R}^{n+1} = \delta_i(\mathbf{F}^+ + \mathbf{F}^-)^{n+1} + \delta_j(\mathbf{G}^+ + \mathbf{G}^-)^{n+1} + \delta_k(\mathbf{H}^+ + \mathbf{H}^-)^{n+1} \quad (6)$$

Linearization of the above split-fluxes, results in the following definitions for the split-flux Jacobians:

$$(\mathbf{A}^\pm) = \left( \frac{\partial \mathbf{F}^\pm}{\partial \mathbf{q}} \right)^n, \quad (\mathbf{B}^\pm) = \left( \frac{\partial \mathbf{G}^\pm}{\partial \mathbf{q}} \right)^n, \quad (\mathbf{C}^\pm) = \left( \frac{\partial \mathbf{H}^\pm}{\partial \mathbf{q}} \right)^n \quad (7)$$

Using these relations, and applying Euler time-integration to (2) yields (11)

$$[\mathbf{I} + \Delta \tau \mathbf{M}^n] \Delta \mathbf{q}^n = - \Delta \tau \mathbf{R}^n \quad (8)$$

where

$$\begin{aligned} \mathbf{M} &= (\delta_i \mathbf{A}^+ + \delta_j \mathbf{B}^+ + \delta_k \mathbf{C}^+) + (\delta_i \mathbf{A}^- + \delta_j \mathbf{B}^- + \delta_k \mathbf{C}^-) \\ &= \mathbf{M}^+ + \mathbf{M}^- \end{aligned} \quad (9)$$

The "dot" appearing after each split-flux Jacobian indicates that the difference operator includes the matrix-vector multiply. Dividing by  $\Delta \tau$ , expanding the difference operators, and regrouping terms yields

$$\mathbf{D}_p \Delta \mathbf{q}_p^n - \mathbf{M}_{p-1}^+ \Delta \mathbf{q}_{p-1}^n + \mathbf{M}_{p+1}^- \Delta \mathbf{q}_{p+1}^n = - \mathbf{R}_p \quad (10)$$

$$\mathbf{D} = \frac{\mathbf{I}}{\Delta \tau} + \mathbf{M}^+ - \mathbf{M}^-$$

at each cell,  $p$ , where the index  $p$  represents the point in three-dimensional computational space corresponding to the point  $(i,j,k)$ . Subscript  $p+1$  correspond to points  $(i+1,j,k)$ ,  $(i,j+1,k)$  and  $(i,j,k+1)$ . Analogous convention is used for the subscript  $p-1$ .

Examining (10) it is apparent that the assembled linearized system is composed of a block diagonal ( $\mathbf{D}$ ), a lower block triangular ( $\mathbf{L}$ ), and an upper block triangular ( $\mathbf{U}$ ) matrix. The system resulting from applying (10) at each cell is expressed as

$$(\mathbf{L} + \mathbf{D} + \mathbf{U}) \Delta \mathbf{Q} = - \mathbf{R} \quad (11)$$

This linear system is solved by applying one symmetric Gauss-Seidel sweep as

$$\begin{aligned}
 (D + L)\Delta q^{(1)} &= -R \\
 (D + U)\Delta q^{(2)} &= -R - L\Delta q^{(1)} \\
 \Delta q^n &= \Delta q^{(2)}
 \end{aligned}
 \tag{12}$$

This particular algorithm has been referred to as the modified two-pass algorithm and is one of a series of similar algorithms developed during the past decade by Whitfield, et. al. (e.g. 4,5,6).

## Results

### National Launch Systems (NLS) Vehicle :

An extensive bench-marking study is conducted using the NLS vehicle as a test case to establish confidence in CFD simulation capabilities, at MSFC, for this class of flows. The surface grid is generated from the drawings that were used for fabricating the 1/10-scale model tested at MSFC wind tunnel facility. The vehicle consists of a cylindrical/oval payload core with a biconic nose cone. The interstage section connects the payload section to an external tank. Two propulsion modules are attached at the aft body. Two configurations, namely Heavy-Lift Launch Vehicle (HLLV) and Early Heavy-Lift Launch Vehicle (EHLLV), are defined by different rotation of oval section of the payload core (Figures 1-2).

The grid generation process was done by application of the GENIE grid generation tool as developed by Soni<sup>(1)</sup>. Initially a C-type, single-block, volume mesh of 279,292 grid points is generated. It is preferred that the volume mesh is decomposed into several blocks in order to take advantage of the solid-stage storage device (SSD) availability on the CRAY-YMP; the biggest block then determines the memory size required during the flow computation process. For this example, the volume mesh is decomposed into 3 blocks; one for each of the boosters and one covering the core body.

The previously described Euler solver was used to calculate flow past the EHLLV at a Mach number of 1.46 and 6 degrees angle of attack (AOA). Figure 3 shows the Mach contours over the EHLLV, as predicted by UBI. These solutions are in good agreement with the numerical solutions presented in an unpublished report by Thomas Wey and Fred Martin at NASA/JSC, using the OVERFLOW code developed at NASA-Ames Research Center

(Figure 4). OVERFLOW is a combination of ARC3D and F3D, both of which had been used widely at ARC and JSC for external flow computations of the space shuttle vehicle. The code is capable of solving problems with overlapped grids<sup>(10,11)</sup>. Although OVERFLOW solutions are viscous, as opposed to the inviscid solutions obtained by UBI, the general trends predicted by the two codes are similar. However, since the two codes are using two different grid systems, some differences may be due to the grid density.

A second simulation was made at a freestream Mach number at 1.05 and 6 degrees AOA. This configuration was also tested at this operating condition at MSFC with net body force data recorded. Figure 5 represents the calculated distributed force coefficients compared with the measured force coefficients. In this Figure, at each station lengthwise, the force coefficient is integrated circumferentially around the half body to yield a single point which represents the total value at that station.

Using the same configuration, the flow fields ranging from transonic to high supersonic are simulated. The solutions are compared to the shadowgraphs taken during the experiment. Similar trends can be found between the flow patterns predicted by UBI and those from the shadowgraphs (Figures 6-17). On the numerical perspective, at a lower Mach number range, the bow shock standing in front of the nose is more detached and the expansion waves seem more severe at the base of the payload mid-section. At a higher Mach number range, the flow field gets compressed and the compression waves become more defined. This phenomenon, in general, can be seen in the shadowgraph whereas the picture becomes clearer at high supersonic flow since the flow field becomes denser. Furthermore, the flow angles over the compression and expansion corners are in good agreement between the simulation and the experiment.

### Single-Stage-To-Orbit (SSTO) Applications:

The objective of this study is to provide surface pressure distributions which can be used for loading analysis during the conceptual design phase. Several lifting body concepts were considered for the SSTO study. Among those, two configurations with distinct shapes and sizes are selected for presentations, herein. The first body is cylindrical with an elliptic nose and the second is delta-shaped with a flat bottom and a wider span

(Figure 18). UBI is used to predict the flow field over these lifting bodies at landing condition ( $Mach=0.5$  and  $\alpha=6$  degrees). The results indicate that the later configuration is more acceptable since it yields a higher lift coefficient ( $Cl=0.6$ ) as compared to the cylindrical body ( $Cl=0.3$ ).

Finally a complete SSTO vehicle with wings and winglets is considered. This vehicle is MSFC modified version of one of the design concepts originated from the Access-to-Space study conducted at NASA Langley Research Center <sup>(12)</sup>.

The GENIE tool was again used for the grid generation about the various SSTO vehicles. The volume grid of the complete SSTO wing-body configuration consists of 4 blocks: block 1 is below the wing, block 2 is above the wing and extends from the body to the winglet, block 3 is also above the wing and extends from the other side of the winglet to farfield, and block 4 is what could have been the sting. This extra block behind the vehicle base is created on purpose, for future study of plume expansion. The four computational blocks totaling 223,720 grid points are shown in Figure 19.

Figure 20 shows particle traces on the vehicle surface, simulated at a Mach number of 0.5 and 12 degrees AOA. This solution is obtained using third-order spatial accuracy. Simulations were also made at Mach numbers of 0.9 and 1.5 at an AOA of five degrees. Symmetry plane Mach number contours for each of these cases are presented in Figures 21 and 22, respectively.

### Conclusions

External flow over several launch vehicle configurations are computed using a high-resolution, finite-volume scheme. Reasonable agreement was demonstrated relative to available experimental data. The scheme is also used to obtain aerodynamic information on different lifting body concepts. The landing lift coefficients resulting from the scheme will determine if a certain lifting body meets the required criteria for landing.

The objective of computing the surface pressure distributions over a launch vehicle configuration has been met. These pressure distributions are what determine the lifting and loading performance of the vehicle. The numerical results obtained can

be used as a data base for other preliminary conceptual designs.

### Acknowledgments

The authors would like to thank Mr. Anthony Springer at MSFC for providing the shadowgraphs. Special acknowledgment is addressed to Dr. Pieter Buning at NASA/ARC for sharing his technical expertise in external flow computations. Appreciation is also expressed to Dr. Hugh Thornburg at Mississippi State University, Engineering Research Center, for his assistance in generating the SSTO grids.

### References

1. Soni, B.K., Thompson, J.F., Stokes, M., and Shih, M.H., "GENIE++, EAGLE View and TIGER: General and Special Purpose Graphically Interactive Grid Systems," AIAA 92-0071, January 1992.
2. Chakravarthy, S.R., and Osher, S., "A New Class of High Accuracy TVD Schemes for Hyperbolic Conservation Laws," AIAA 85-1703, January 1985.
3. Whitfield, D.L., "Implicit Upwind Finite Volume Scheme for the Three-Dimensional Euler Equations," Engineering and Industrial Research Station Report MSSU-EIRS-ASE-85-1, Mississippi State University, September 1985.
4. Whitfield, D.L. and Janus, J.M., "Implicit Finite Volume Scheme Wave-Split Scheme for Solving the Unsteady Three-Dimensional Euler and Navier-Stokes Equations on Stationary or Dynamic Grids," Engineering and Industrial Research Station Report MSSU-EIRS-ASE-88-2, Mississippi State University, February 1988.
5. Whitfield, D.L., Janus, J.M., and Arabshahi, A., "Unsteady Euler Solutions on Dynamic Block Grids for Complex Configurations," AGARD Conference Proceedings, No. 464, 1990.
6. Hirsch, C., "Numerical Computation of Internal and External Flows, Volume 2: Computational Methods for Inviscid and Viscous Flows," John Wiley and Sons, New York, 1988, pp. 132-135.

7. Osher, S. and Chakravarthy, S., "Very High Order Accurate TVD Schemes," ICASE Report No. 84-44, Sept. 1984.

8. Steger, J.L., and Warming, R.F., "Flux Vector Splitting of the Inviscid Gasdynamic Equations with Application to Finite-Difference Methods," Journal of Computational Physics, Vol. 43, 1981, pp. 357-372.

9. Roe, P.L., "Approximate Riemann Solvers, Parameter Vectors, and Difference Schemes," Journal of Computational Physics, Vol. 43, 1981, pp. 357-372.

10. Buning, P.G., et. al., "OVERFLOW User's Manual, Version 1.6p," NASA Ames Research Center, Moffett Field, CA, December 1991.

11. Benek, J.A., Buning, P.G., and Steger, J.L., "A 3-D Grid Embedding Technique," AIAA-85-1523-CP, July 1985.

12. "Access-To-Space Advanced Technology Team Final Report, Option 3," Final Report, Volume 3, Design Data Book, NASA Langley Research Center, Hampton, VA, July 1993.

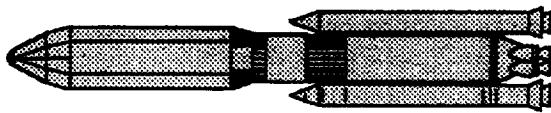


Figure 1. Early HLLV configuration

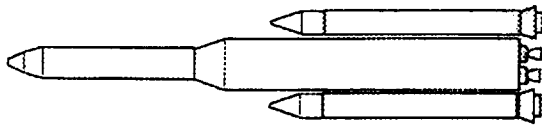


Figure 2. HLLV configuration

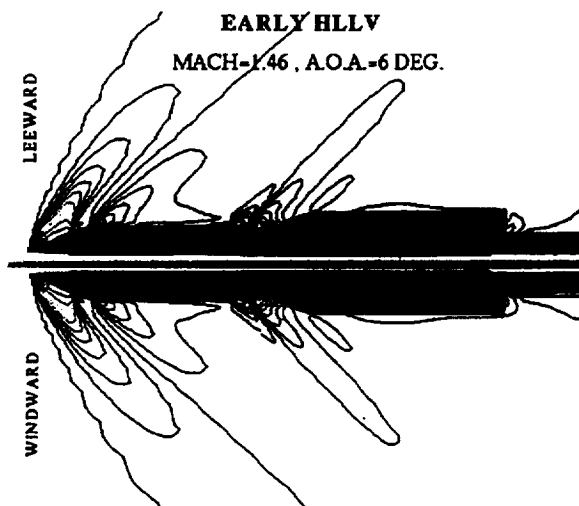


Figure 3. UBI solution ( $M_\infty = 1.46$ ,  $\alpha = 0^\circ$ )

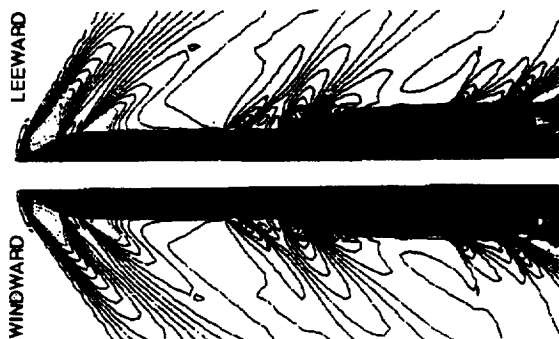


Figure 4. OVERFLOW solution ( $M_\infty = 1.46$ ,  $\alpha = 0^\circ$ )

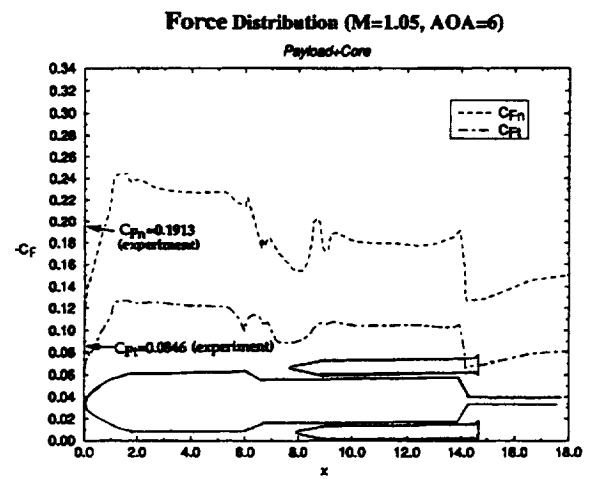


Figure 5. Surface Forces ( $M_\infty = 1.05$ ,  $\alpha = 6^\circ$ )

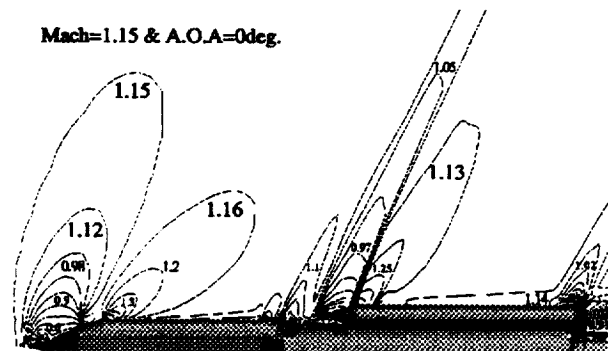


Figure 6. Numerical solution ( $M_\infty = 1.15$  &  $\alpha = 0^\circ$ )

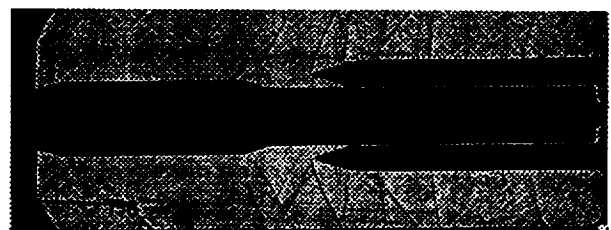
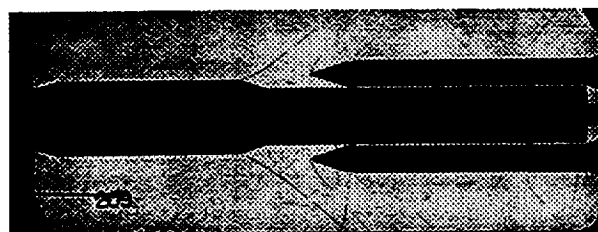
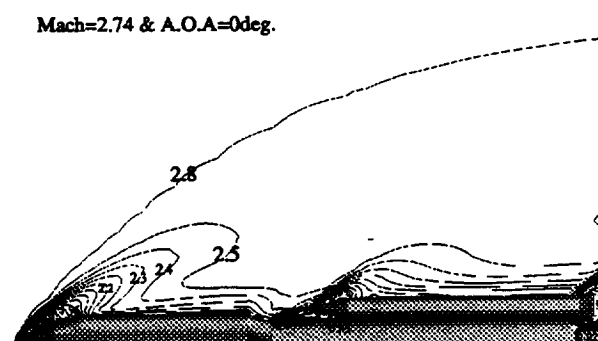
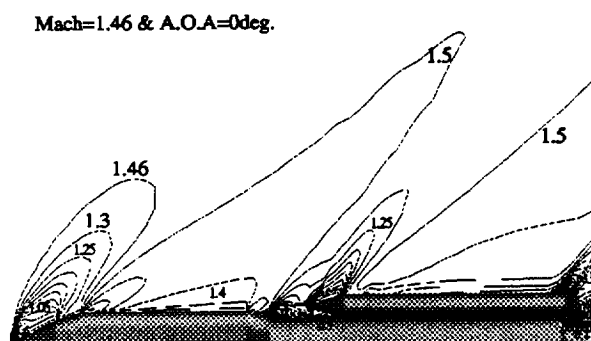
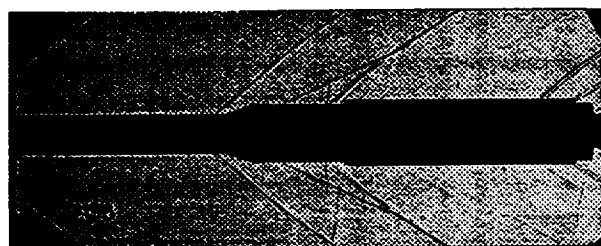
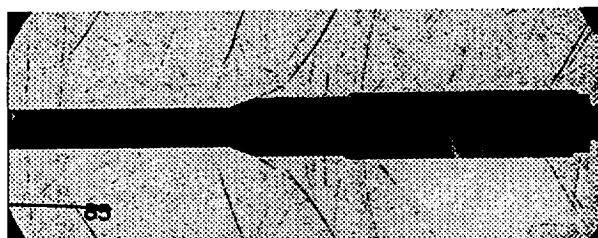
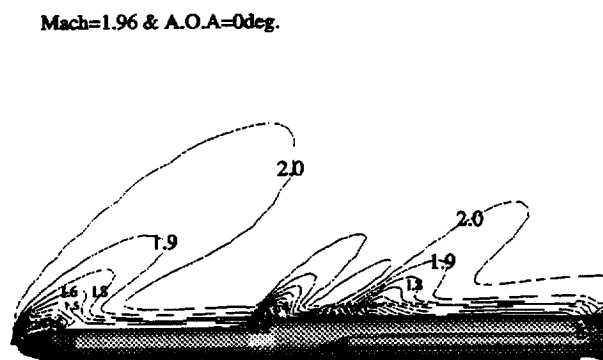
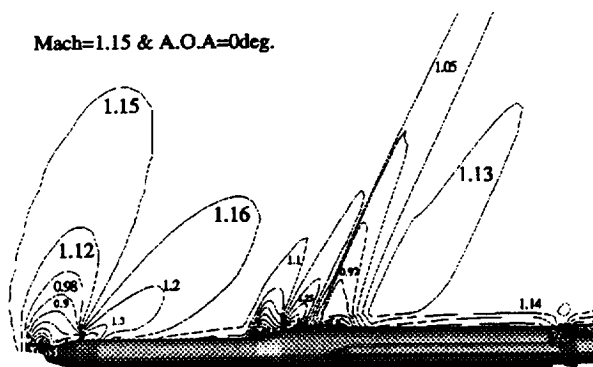


Figure 7. Shadowgraph ( $M_\infty = 1.15$  &  $\alpha = 0^\circ$ )





Mach=2.74 & A.O.A=0deg.

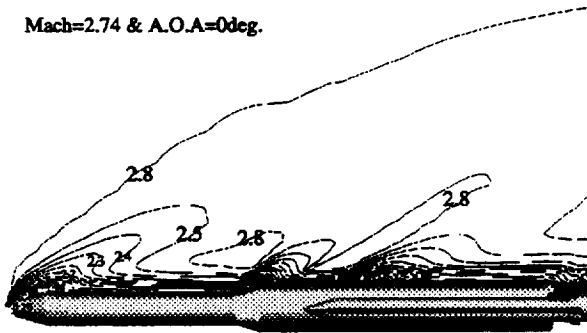


Figure 16. Numerical solution ( $M_{\infty}=2.74$ ,  $\alpha=0^{\circ}$ )

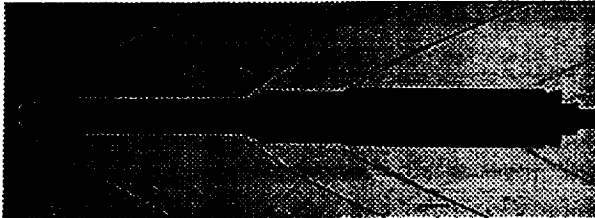


Figure 17. Shadowgraph ( $M_{\infty}=2.74$ ,  $\alpha=0^{\circ}$ )

Lifting Body Concepts  
Mach = 0.5 A.O.A = 12 degrees

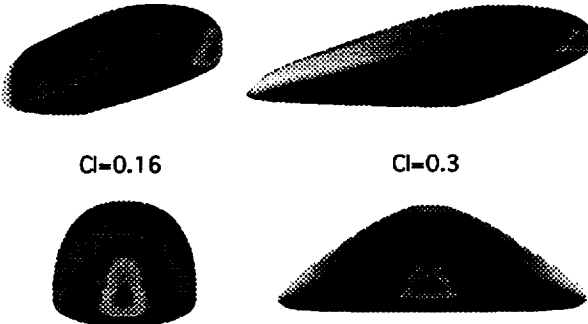


Figure 18. Landing simulation of lifting bodies

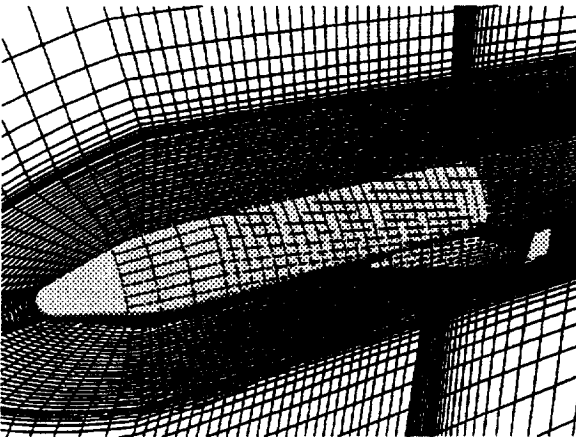


Figure 19. SSTO vehicle configuration

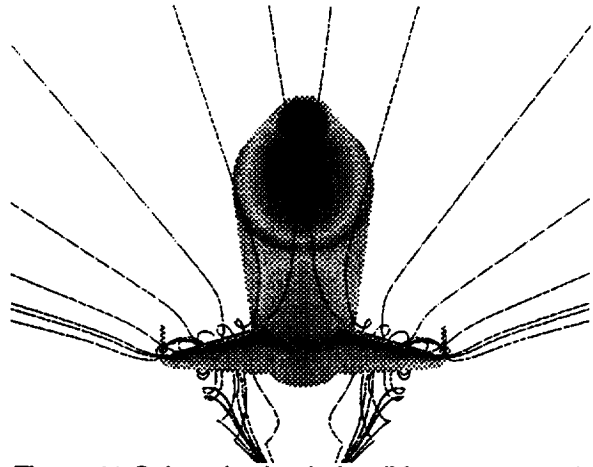


Figure 20 Subsonic simulation ( $M_{\infty}=0.5$ ,  $\alpha=12^{\circ}$ )

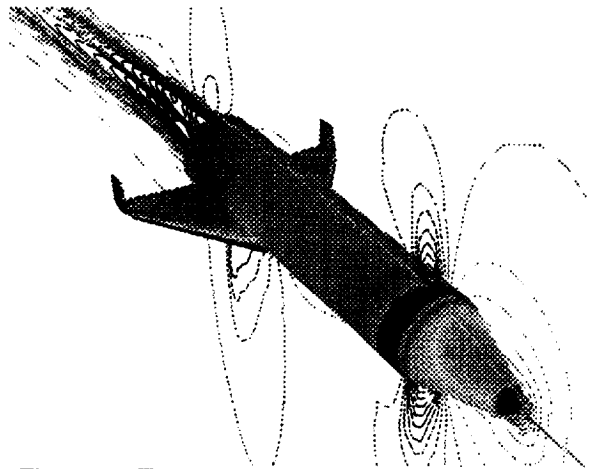


Figure 21 Transonic simulation ( $M_{\infty}=0.9$ ,  $\alpha=5^{\circ}$ )

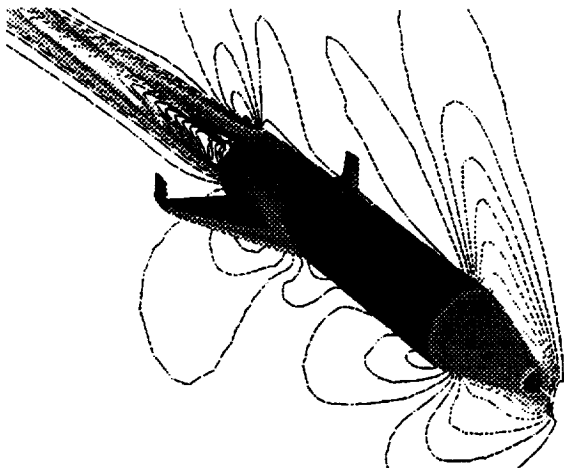


Figure 22 Supersonic simulation ( $M_{\infty}=1.5$ ,  $\alpha=5^{\circ}$ )